RSC Advances

ROYAL SOCIETY OF CHEMISTRY

PAPER

View Article Online
View Journal | View Issue

Cite this: *RSC Adv.*, 2026, **16**, 1714

Mn^{2+}-assisted high-capacity retention in iron–chromium flow batteries *via* hydrogen evolution inhibition and Cr^{3+}/Cr^{2+} activation

Tian-Ying Zhang,[ab] Zheng-Rong Niu,[c] Bo Li,[c] Yuan-Yuan Cui,[d] Nai-Cai Xu, *[ab] Xin-Qian Li,[c] Shao-Ju Bian,[ab] Ya-Ping Dong,[c] Hai-Tao Feng*[c] and Yan-Feng Gao *[d]

The iron–chromium redox flow battery (ICRFB) has emerged as one of the most promising technologies for large-scale energy storage systems. At the same time, the parasitic hydrogen evolution reaction (HER) during the negative process remains a challenge for the long-term operation. To solve this issue, Mn^{2+} is used as an additive to enhance the stability and performance of ICRFBs. The results demonstrate that Mn^{2+} not only effectively inhibits HER but also accelerates the kinetics of Cr^{3+}/Cr^{2+} and Fe^{3+}/Fe^{2+} to some extent. Notably, the introduction of 0.002 M Mn^{2+} into the electrolyte significantly enhanced the coulombic efficiency (CE) and capacity retention of the battery. Specifically, at a current density of 40 mA cm^{-2}, the CE increased from 96.34% to 97.15%. Furthermore, after 100 long-term cycles, the Mn^{2+}-modified electrolyte retained 73% of its initial discharge capacity, whereas the pristine electrolyte exhibited only 39% retention. This performance enhancement can be attributed to two key mechanisms. The negative shift of the hydrogenation potential induced by Mn^{2+} doping effectively inhibits the hydrogenation side reaction, and this result is also verified in the DFT (Density Functional Theory) calculations. The Mn^{2+} in the solution increases the electrochemical activity of the reaction system, thereby reducing the degradation of the electrolyte. These findings provide critical insights into the design of effective electrolyte additives for high-performance ICRFBs, highlighting Mn^{2+} as a promising candidate for mitigating capacity fade and improving overall electrochemical efficiency.

Received 22nd November 2025
Accepted 26th December 2025

DOI: 10.1039/d5ra09027j

rsc.li/rsc-advances

1 Introduction

The utilization of electricity derived from renewable energy sources is widely considered an effective solution to address the escalating energy requirements and mounting environmental concerns.[1,2] However, the intermittent nature of renewable resources gives rise to an unstable energy supply and unsatisfactory energy density, which strictly confines their further application in energy storage.[3] It is imperative to acknowledge the escalating demand for clean energy, which necessitates the incorporation of innovative energy storage technologies to address the intermittent and variable nature of renewable energy sources.[4–6]

Redox flow batteries (RFBs) are a promising technological solution for large-scale energy storage, due their inherent scalability, longevity and decoupled energy-power design. Different kinds of redox flow battery technologies have been developed since the 1970s, which include all vanadium redox flow batteries (VRBs),[7] iron chromium redox flow batteries (ICRFBs),[8] and zinc-bromine redox flow batteries (ZBRFBs).[9] Among various RFBs, the ICRFB has garnered renewed interest due to the natural abundance, low cost, and environmental benignity of its active materials (Fe^{3+}/Fe^{2+} and Cr^{3+}/Cr^{2+} redox couples).[10,11] The electrode reactions of the ICRFB are as follows:

$$\text{Positive electrode}: \quad Fe^{2+} \underset{\text{discharge}}{\overset{\text{charge}}{\longleftrightarrow}} Fe^{3+} + e, \quad \phi = 0.77 \text{ V}$$

$$\text{Negative electrode}: \quad Cr^{3+} + e \underset{\text{discharge}}{\overset{\text{charge}}{\longleftrightarrow}} Cr^{2+}, \quad \phi = -0.41 \text{ V}$$

$$\text{Overall reaction}: \quad Fe^{2+} + Cr^{3+} \underset{\text{discharge}}{\overset{\text{charge}}{\longleftrightarrow}} Cr^{2+} + Fe^{3+}, \quad \phi = 1.18 \text{ V}$$

[a]*School of Chemistry and Chemical Engineering, Qinghai Normal University, Xining 810008, China. E-mail: xunc@qhnu.edu.cn*

[b]*Qinghai Key Laboratory of Advanced Technology and Application of Environmental Functional Materials, Xining 810016, China*

[c]*Key Laboratory of Green and High-end Utilization of Salt Lake Resources, Qinghai Engineering and Technology Research Center of Comprehensive Utilization of Salt Lake Resources, Qinghai Institute of Salt Lakes, Chinese Academy of Sciences, Xining, Qinghai 810008, China. E-mail: fenght@isl.ac.cn*

[d]*School of Materials Science and Engineering, Shanghai University, Shanghai, China. E-mail: yfgao@shu.edu.cn*

However, the commercialization of ICRFB has been hindered by several persistent challenges, including sluggish reaction kinetics, low reversibility of the Cr^{3+}/Cr^{2+}, and crossover-induced capacity decay. These limitations collectively degrade energy efficiency (EE) and cycling stability, necessitating innovative strategies to enhance electrode kinetics and mitigate side reactions. Recent efforts to improve ICRFB performance have focused on optimizing electrolyte composition, modifying electrode surfaces, and introducing electrocatalytic additives. Zhang *et al.*[12] prepared a modified graphite felt (GF) electrode with polyacrylonitrile (PAN) and artificial fiber as precursors, which improved the conductivity and electrochemical activity of the reaction system. Niu *et al.*[13] designed and prepared N–B co-doped coupling TiB_2 composite electrode, which provided abundant reaction sites and accelerated the diffusion rate of reactants. In addition, it also promotes electron transfer and enhances the physical and chemical properties of the electrode. Che *et al.*[14] prepared amorphous bismuth nanoparticles (NPs) and immobilised them on nitrogen-doped GF, which significantly improved electrochemical activity and reduced charge transfer resistance. Niu *et al.*[15] fabricated a defect-rich carbon cloth electrode *via* silicic acid etching, achieving a robust nanoporous structure with enhanced active sites. The fabricated electrode exhibits abundant defect sites and excellent electron transport properties.

In conclusion, these electrode modification methods effectively improve the performance of ICRFB. Generally, Nafion proton exchange membranes are widely used in ICRFB but suffer from high cost and low ion selectivity. Recent developments in membrane materials for ICRFB have identified two particularly promising alternatives: sulfonated poly (ether ether ketone) (SPEEK)[16] and Sulfonated polybenzimidazole (SPBI).[17] These polymer-based membranes demonstrate superior performance characteristics compared to conventional materials. Furthermore, researchers have achieved additional performance enhancements through strategic incorporation of nanoscale additives, with carbon nanotubes (CNTs) showing particularly notable improvements in membrane properties.[18] Li *et al.*[19] successfully prepared a series of polyaniline (PANI) composite ion-exchange membranes by incorporating PANI nanotubes into Nafion at varying doping levels. This modification improved membrane water retention, dimensional stability, and proton conductivity. These studies provide insights for optimizing ion-conducting membranes for improved ICRFB performance. Despite the noteworthy advancements in the field of electrode material and ionic membrane modification, there is a conspicuous absence of a modification scheme that has demonstrated manifest advantages in commercial applications. This is primarily attributable to the cumbersome treatment process, the limited enhancement in electrochemical performance, and the suboptimal cycle stability. It is imperative to devise a straightforward yet effective approach to enhance the overall performance and durability of ICRFB. With good tunability and scalability, electrolyte optimization is a practical and cost-effective solution for advancing ICRFB technology by directly influencing key parameters such as ion transport, conductivity, and redox activity.[20] This approach presents a cost-effective pathway for advancing ICRFB technology.[21,22] Recent studies demonstrate that additive engineering can significantly enhance electrolyte performance through distinct mechanisms.[23–25] Inorganic additives: Wang *et al.*[26] demonstrated that In^{3+} incorporation in the anolyte achieves dual functionality-suppressing the hydrogen evolution reaction (HER) while simultaneously enhancing Cr^{3+}/Cr^{2+} redox kinetics, leading to improved battery efficiency. Organic chelators: EDTA and PDTA additives effectively prevent metal ion hydrolysis through complexation with Cr^{3+} and Fe^{2+}. Particularly noteworthy is Niu *et al.*[27] chromium-diethylenetriaminepentaacetic acid complex (CrDTPA), which exhibits remarkable cycling stability with minimal capacity fade. Nitrogen-containing organics: Deng *et al.*[28] investigated imidazole-based additives (L-histidine and 2-methylimidazole), showing significant improvements in both coulombic efficiency (CE) and cycle life.

To summaries, the integration of additives into the electrolyte constitutes a straightforward and efficacious approach to enhance the sluggish reaction kinetics of Cr^{3+}/Cr^{2+}. Consequently, this method leads to an augmentation in the performance and cycle life of ICRFB. Notably, manganese ions have shown potential as multifunctional mediators in aqueous electrochemical systems due to their favorable redox properties, high solubility, and catalytic activity. This study proposes Mn^{2+} ion doping in ICRFB electrolytes as a novel strategy to simultaneously overcome kinetic limitations and enhance battery cycle stability. The rationale hinges on the dual role of Mn^{2+}, is acts as a redox mediator to facilitate electron transfer at the Cr electrode, thereby improving the reversibility of the Cr^{3+}/Cr^{2+} couple. Furthermore, Mn^{2+} may stabilize the electrolyte environment by mitigating hydrogen evolution and parasitic reactions at low potentials, which is crucial for maintaining battery performance.

2 Materials and methods

2.1. Experimental reagents and instruments

The chemicals and apparatus are listed in Table 1 and 2. The pristine electrolyte (1.0 M $FeCl_2$, 1.0 M $CrCl_3$, and 3.0 M HCl) was prepared by dissolving $FeCl_2 \cdot 4H_2O$ and $CrCl_3 \cdot 6H_2O$ in deionized water, adding concentrated HCl, and diluting to volume under continuous stirring at room temperature. Mn^{2+}-containing electrolytes were obtained by adding $MnCl_2 \cdot 4H_2O$ to the base solution and diluting accordingly. All electrolytes were equilibrated for 2 h before use, and the glass fiber separator and ion-exchange membrane were replaced after each experiment.

2.2. Electrochemical measurements

A single flow cell was assembled using Nafion212 as the membrane and copper-coated carbon-plastic composite as bipolar plates. The electrodes consisted of PAN-based glass fiber felts (4.6 mm thickness, 40 mm × 130 mm) (Wuhan Chuxin Technology Co., Ltd China) embedded in polypropylene frames. The catholyte and anolyte (50 mL each) were circulated at 50

Table 1 Chemical reagents used in the experiments

Chemical name	Molecular formula	Purity/Grade	Supplier
Chromium(III) chloride hexahydrate	$CrCl_3 \cdot 6H_2O$	AR	Macklin
Iron(II) chloride tetrahydrate	$FeCl_2 \cdot 4H_2O$	AR	Sinopharm Chemical Reagent Co., Ltd
Hydrochloric acid	HCl	AR	Sichuan Xilong Scientific Co., Ltd
Manganese(II) chloride tetrahydrate	$MnCl_2 \cdot 4H_2O$	AR	Tianjin Double Ship Chemical Reagent Factory

Table 2 Laboratory apparatus in this work

Name	Instrument types	Manufacturer/Supplier
Peristaltic pump	DIPump550	Wuhan Chuxin Technology Co., Ltd. (China)
Ultra-pure water equipment	UPH-I-80L	Sichuan UP Ultra-Pure Technology Co., Ltd. (China)
Analytical balance	BSA623S-CW	Sartorius Scientific Instruments (Beijing) Co., Ltd. (China)
Magnetic stirrer	DF-101S	Gongyi Yuhua Instrument Co., Ltd. (China)
Electrochemical workstation	PGSTAT128N	Metrohm China Ltd. (Switzerland)
Ionic membrane	Nafion212	Wuhan Chuxin Technology Co., Ltd. (China)

mL min^{-1}. Galvanostatic charge–discharge tests were conducted within a current density range of 30–55 mA cm^{-2} (corresponding voltage window: 0.5–1.2 V), with cycling stability evaluated at 40 mA cm^{-2}. Electrochemical measurements, including cyclic voltammetry (CV) and electrochemical impedance spectroscopy (EIS), were performed on a Metrohm PGSTAT128N using a standard three-electrode configuration with a glassy carbon working electrode, a platinum counter electrode, and a saturated calomel reference electrode (SCE). For glassy carbon electrodes used in CV/LSV testing within a three-electrode system, the pretreatment procedure was as follows: Prior to use, the electrodes were sequentially polished to a mirror finish on chamois using 0.3 μm and 0.05 μm alumina polishing powder, then rinsed with deionized water and set aside for later use.

2.3. Material characterizations

The viscosity and conductivity of the electrolytes were measured at room temperature using a flat Ubbelohde viscometer (Model 1835A) and a conductivity meter (S230-K, Mettler-Toledo). Each sample was subjected to three independent tests, and the mean value was documented. The electrode morphology was examined before and after cycling by means of scanning electron microscopy (JSM-5610LV). Elemental composition was analyzed by means of a scanning electron microscope (SEM) equipped with an energy-dispersive X-ray spectroscopy (EDS, X-MAXN) system. The surface chemical states of GF were characterized in further detail by X-ray photoelectron spectroscopy (XPS, 156 Kratos Axis Supra$^+$) with Mg Kα radiation.

2.4. Computational details

The DFT (Density Functional Theory) calculations were performed with VASP. Exchange–correlation was treated with the PBE functional, and core-valence interactions were described by PAW pseudopotentials. A plane-wave cutoff of 520 eV was adopted. A defect-free graphite (001) slab, 3 × 3 in-plane supercell, 4 layers thick, and separated by 15 Å of vacuum, served as the electrode model. The bottom 2 layers were fixed at

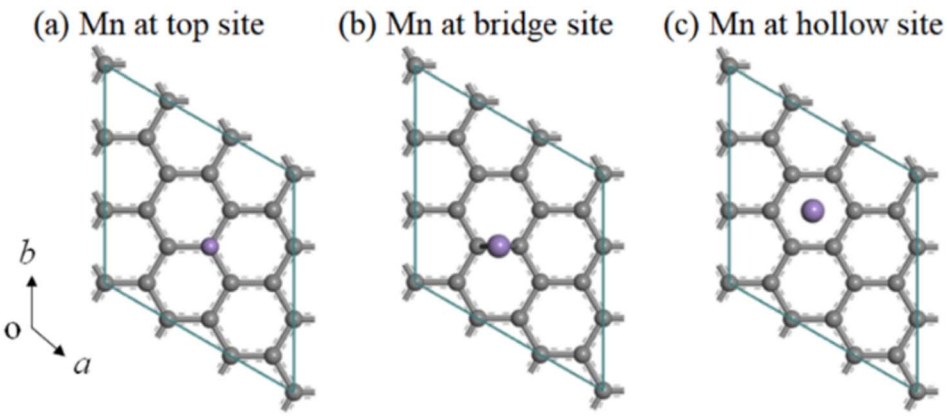

Fig. 1 The top view of one Mn atom absorbed on the surface of graphite. (a) Mn at the top of one carbon atom, (b) Mn at the bridge site of two carbon atoms, and (c) Mn at the hollow site of six carbon atoms. The gray balls are for the carbon atoms, and the purple balls are for the Mn atoms.

bulk positions. Γ-Centered *k*-meshes of 3 × 3 × 1 ensured convergence to less than 1.0 × 10^{-4} eV. The Mn sites were evaluated for the top, bridge, and hollow sites to identify the most stable configuration (Fig. 1). The HER pathways were calculated on three systems, *i.e.*, the bare graphite, the Mn-adsorbed graphite, and the Mn–Cr co-adsorbed graphite.

3 Results and discussion

3.1. Electrolyte performance tests

Conductivity serves as a critical parameter for evaluating the ionic transport properties of electrolytes,[29] directly influencing key battery performance metrics including charge–discharge efficiency, power output, and energy conversion efficiency. Elevated electrolyte conductivity enhances ion mobility, minimizes ohmic polarization, and reduces energy dissipation, thereby improving overall cell performance. To investigate the role of Mn^{2+} in modulating these characteristics, we systematically measured the electrolyte conductivity across varying Mn^{2+} concentrations (Fig. 2).

The results showed that as the Mn^{2+} concentration increased, the conductivity enhanced. The conductivity increased from 305 mS cm^{-1} at 0 M Mn^{2+} to 312 mS cm^{-1} at 0.01 M Mn^{2+}, reflecting a 2.3% improvement. This trend indicates that the incorporation of Mn^{2+} promotes ion transport within the electrolyte. To systematically evaluate the influence of Mn^{2+} concentration on electrochemical performance, galvanostatic charge–discharge cycling was performed using electrolytes with varying Mn^{2+} concentrations.

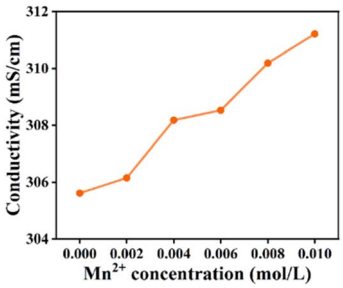

Fig. 2 The conductivity of the electrolyte at different Mn^{2+} concentrations.

An investigation was conducted into the impact of Mn^{2+} addition (in increments of 0 to 0.01 M, at 0.002 M intervals) on the battery's performance, with the objective of enhancing electrochemical efficiency. The evaluation of the charge–discharge capacity, the CE, the EE, and the voltage efficiency (VE) was conducted at a current density of 40 mA cm^{-2}. As illustrated in Fig. 3a and b, the incorporation of 0.002 M Mn^{2+} into the electrolyte resulted in a substantial enhancement in charge and discharge capacities, with an increase of 2.2% and 1.5%, respectively, in comparison with the pristine electrolyte. This enhancement can be attributed to the catalytic effect of low-concentration Mn^{2+}, which accelerates the electrochemical reaction kinetics while suppressing HER, thereby improving active species utilization. The increase in the concentration of Mn^{2+} led to a gradual decrease in the charging and discharging capacity of the battery, this may be due to increased polarization as Mn^{2+} concentration rises. As shown in Fig. 3c–e, specifically, at a current density of 40 mA cm^{-2}, CE increases from 96.34% to 97.15%, while the energy efficiency improves from 79.51% to 80.37%. Similarly, the VE exhibits an enhancement from 82.55% to 82.74%.

Results indicate that the 0.002 M sample exhibits superior capacity retention during extended cycling, while evaluating three key battery efficiencies: CE, EE, and VE. In contrast, the 0.002 M sample demonstrates a more balanced and sustainable performance profile between efficiency metrics and capacity stability. Consequently, we ultimately selected 0.002 M Mn^{2+} as the subject for subsequent in-depth investigation.

The voltage–capacity profiles in Fig. 3f demonstrate that the addition of 0.002 M Mn^{2+} improves battery efficiency, it was

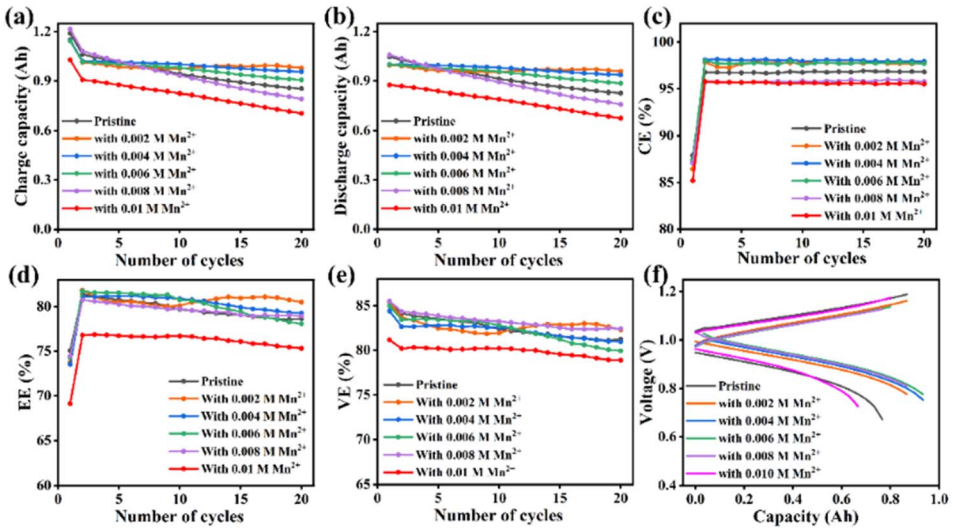

Fig. 3 Effects of concentration of Mn^{2+} on ICRFB performance: (a) charge and (b) discharge capacity diagram; (c) CE; (d) EE; (e) VE; (f) capacitance–voltage curve at 40 mA cm^{-2}.

observed that there was a higher discharge voltage plateau and a lower charge voltage plateau in this system in comparison to the Mn^{2+}-free system. This indicates that the introduction of Mn^{2+} into the electrolyte can improve the VE of ICRFB. These results indicate that Mn^{2+} at an optimal concentration (0.002 M) facilitates redox kinetics and reduces polarization. By comparing the voltage differences between charge and discharge plateaus, polarization conditions at different concentrations can be elucidated. Details of curve shape: Note the abnormal upward deflection at the end of the charging curve for the 0.01 M sample (potentially indicating severe concentration polarization or side reactions). As Mn^{2+} concentration increases, the gap between charge and discharge plateaus widens, indicating heightened polarization. This provides strong evidence for the performance decline at 0.01 M Mn^{2+}.

The electrochemical behavior of electrolytes containing Mn^{2+} was investigated in this study using CV. CV measurements were performed by means of a graphite electrode in the electrolyte, with and without the presence of Mn^{2+}. The CV scans were conducted at a scan rate of 10 mV s^{-1}, encompassing potential windows from −1 to 0 V (relative to the reference electrode) for the cathodic process and from 0 to 1 V for the anodic process. Furthermore, EIS was conducted within a frequency range spanning from 100 kHz to 0.01 Hz, employing a scanning amplitude of 10 mV at a DC voltage of 0.5 V.

In the pristine electrolyte, the Fe^{3+}/Fe^{2+} couple exhibited a ΔE_p of 144 mV and a $-I_{pa}/I_{pc}$ ratio of 1.187. After adding 0.002 M Mn^{2+}, ΔE_p decreased slightly to 141 mV and the $-I_{pa}/I_{pc}$ ratio decreased to 1.184. The smaller ΔE_p and the ratio closer to 1 indicate enhanced electrochemical activity of the Fe^{3+}/Fe^{2+} couple in the Mn^{2+}-modified electrolyte. For the Cr^{3+}/Cr^{2+} couple, the anodic peak current (I_{Pa}) increased upon Mn^{2+} addition, further confirming improved electrochemical activity in the presence of 0.002 M Mn^{2+}. This result demonstrates that Mn^{2+} concentration plays a critical role in governing the reaction dynamics (Fig. 4a and b).

To further investigate the influence of Mn^{2+} on HER in batteries, linear sweep voltammetry (LSV) was systematically conducted. As shown in Fig. 4d, the LSV analysis reveals that the incorporation of Mn^{2+} induces a cathodic shift in HER onset potential. The reduction of Cr^{3+} is initiated at a scan potential of −0.5 V, in comparison to the electrolyte in its pristine state, the introduction of 0.002 M Mn^{2+} results in a positive shift in the Cr^{3+}/Cr^{2+} redox potential, indicating enhanced electrochemical activity and a facilitated reduction process. In order to further observe the change of LSV, region 1 and region 2 in Fig. 4d are enlarged, and the results are shown in Fig. 4e and f. As shown in Fig. 4e, after further lowering the potential, a sharp increase in current density is observed at the characteristic potential, marking the onset of HER, which is consistent with the HER behavior of the electrolyte. It is worth noting that, compared to the original electrolyte (−0.90 V), the electrolyte containing Mn^{2+} exhibits a more negative HER onset potential (−0.95 V). This cathodic shift indicates that Mn^{2+} effectively suppresses HER. This finding is also confirmed in Fig. S1 (the gas production change in the 20th cycle for the Mn^{2+}-containing anolyte is significantly smaller than that of the Mn^{2+}-free system). As shown in Fig. 4f, at the same current density (such as 27 mA cm^{-2}), the working potential of the Cr reduction process shifted from approximately −0.76 V to approximately −0.68 V after adding 0.002 M Mn^{2+}, indicating that Mn^{2+} introduction reduces the overpotential of the Cr reduction process. These findings demonstrate that Mn^{2+} acts as

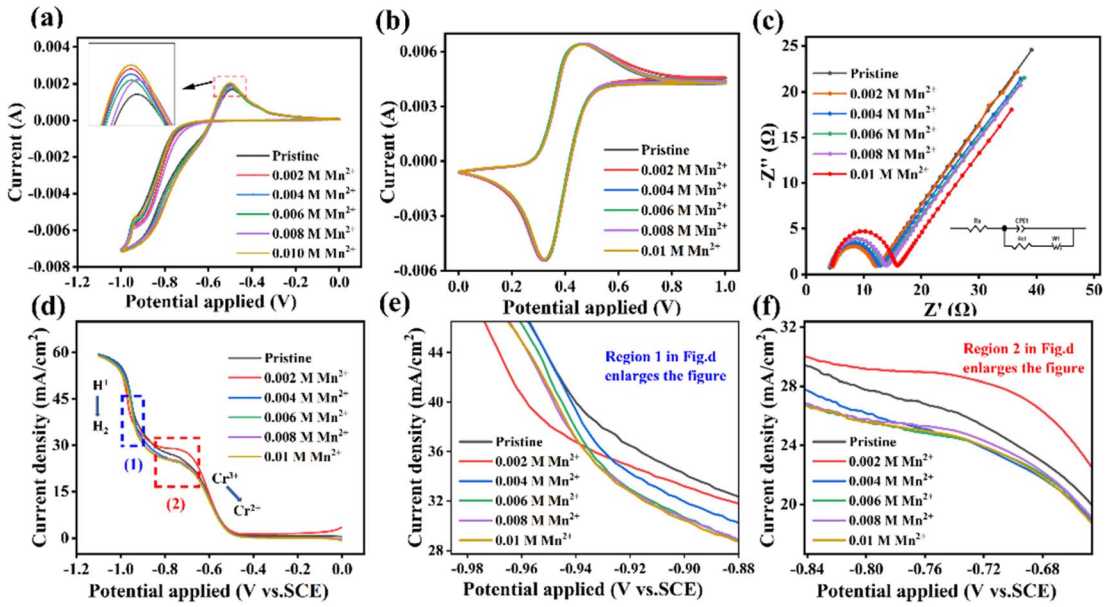

Fig. 4 Effect of Mn^{2+} electrolyte on electrochemical behavior: (a) CV curves at a scan rate of 10 mV s^{-1} between −1 and 0 V; (b) CV curves at a scan rate of 10 mV s^{-1} between 0 and 1 V; (c) Nyquist plot at 0.5 V and the equivalent circuit diagram; (d) linear sweep voltammetry result; (e) d region 1 enlarged figure; (f) d region 2 enlarged figure.

Table 3 Impedance data table of different concentrations of Mn^{2+} electrolyte

Mn^{2+} concentration (mol L^{-1})	0	0.002	0.004	0.006	0.008	0.010
R_s	3.87	3.77	3.69	3.63	3.61	3.59
R_{ct}	8.78	8.54	8.97	9.21	9.31	9.58

a beneficial additive for both inhibiting HER and enhancing the electrochemical activity of the reaction system.

The impact of Mn^{2+} on the electrolyte impedance was measured using EIS from 100 kHz to 0.01 Hz at 0.5 V and 10 mV amplitude. The impedance data were fitted to an equivalent circuit model in ZView to show the electrolyte's impedance characteristics and how Mn^{2+} affects the electrochemical performance (Fig. 4c). The addition of Mn^{2+} altered the electrolyte's impedance. To quantify the influence of Mn^{2+}, ZView was used to extract electrochemical parameters (R_{ct}, R_s) from the EIS data and fit them into the equivalent circuit model. The values of these parameters are in Table 3, showing the impact of Mn^{2+} on the electrochemical dynamics of the electrolyte and the battery's performance.

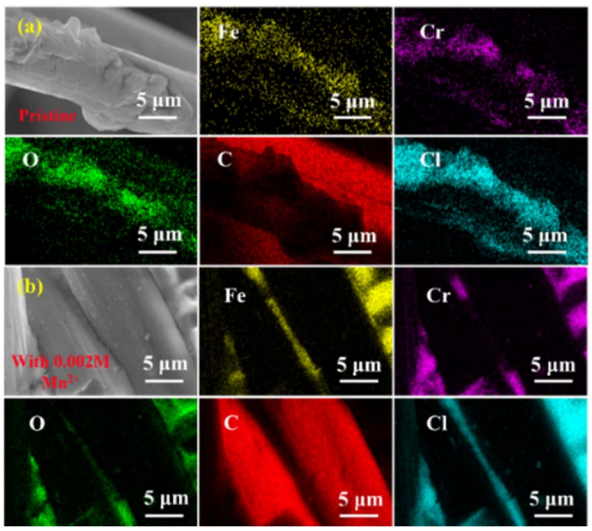

Fig. 5 SEM images and EDS mapping of GFs after charging and discharging using (a) pristine electrolyte and (b) electrolyte containing 0.002 M Mn^{2+}.

Table 3 indicates that as the Mn^{2+} concentration increases from 0 to 0.010 M, R_s gradually decreases from 3.87 Ω to 3.59 Ω, exhibiting an overall linear decline. This suggests that higher Mn^{2+} concentrations significantly suppress R_s, thereby improving the electrolyte's conductivity, reducing voltage losses, and enhancing overall battery efficiency. However, from 0.002 M to 0.010 M, R_{ct} increases from 8.54 Ω to 9.58 Ω, showing a clear upward trend. This indicates that at higher concentrations, Mn^{2+} contributes to an increase in R_{ct}. The initial enhancement in solution conductivity with Mn^{2+} addition may be attributed to its charge-carrying capability, leading to the reduction in R_s. However, at high concentrations, factors such as increased ion interaction or changes in solution viscosity may hinder the ion transfer process, resulting in higher R_{ct}.

The subsequent investigation into the provenance of the observed enhancement in performance involved conducting a series of scans on GF. These scans were performed prior to and following cycles of charging and discharging. The utilization of SEM and EDS in these scans facilitated a detailed and comprehensive analysis. As shown in Fig. 5, comparing the surface morphology analysis before (see Fig. S2) and after cycling reveals that sparse particles adhere to the electrode surface post-cycling. Analysis of these particles indicates strong spatial correlation between C, O, Cl, Fe, and Cr, while Mn is not detected on the electrode surface. The absence of Mn signals in the XPS elemental maps further corroborates this observation (Fig. S3). These results further support that the performance improvement stems from the role of Mn^{2+} in the electrolyte rather than electrode deposition.

This paper builds upon the existing body of research by further investigating the impact of the Mn^{2+} concentration on the charge and discharge processes within ICRFB. To this end, constant current charge and discharge tests were conducted at varying current densities, thereby facilitating a more comprehensive and nuanced understanding of the underlying mechanisms. The electrochemical performance was methodically evaluated at current densities ranging from 30 to 55 mA cm^{-2} in increments of 5 mA cm^{-2}. The CE, EE and VE were measured at these current densities. As demonstrated in Fig. 6a–c, CE increased with current density. In contrast, VE demonstrates a substantial decline at elevated current densities, which is ascribed to the augmented polarization during the charging and discharging processes. It is important to note that, under identical current conditions, specifically at a lower current

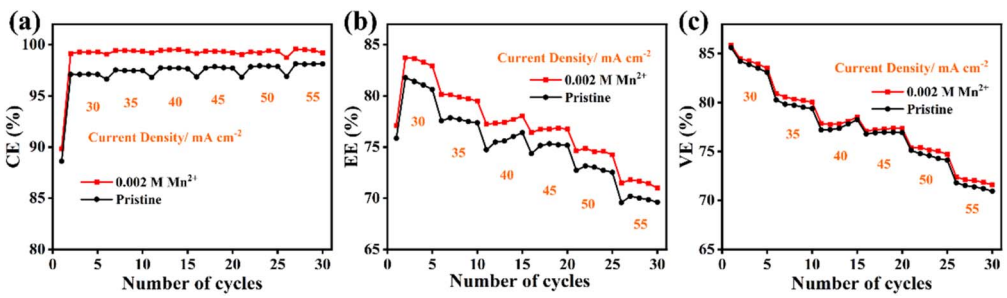

Fig. 6 Discharge capacity *vs.* cycle number at various current densities: (a) CE; (b) EE; (c) VE.

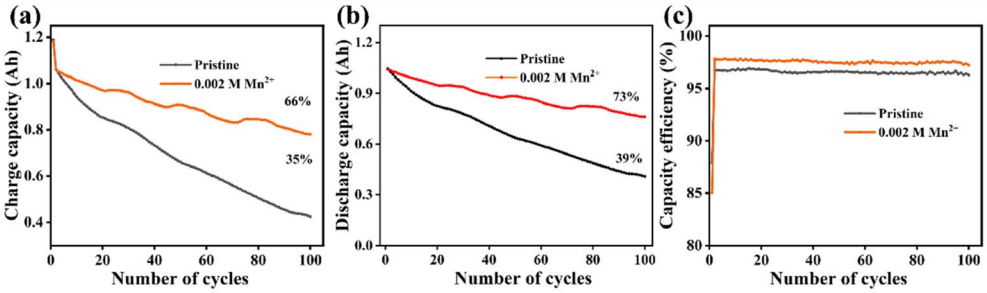

Fig. 7 The cycle performance of ICRFB with and without 0.002 M Mn^{2+} anode electrolyte: (a) charge capacity, (b) discharge capacity, and (c) CE.

density, the CE of the electrolyte containing Mn^{2+} is considerably higher than that of the electrolyte devoid of Mn^{2+}.

CE exhibits excellent stability and minimal fluctuation under all test conditions. Compared with the electrolyte without Mn^{2+}, the CE, VE, and EE with Mn^{2+} were significantly enhanced, indicating that the electrochemical performance was improved, which may be due to the inhibition of parasitic reaction and optimized ionic activity. These results demonstrate that 0.002 M Mn^{2+} incorporation significantly enhances cycling stability and overall cell performance, highlighting its promise as an effective electrolyte additive for rechargeable battery systems.

In order to perform a more comprehensive evaluation of the long-term cycle stability of ICRFB, a constant current cycle test was conducted at a current density of 40 mA cm^{-2}. A comparative study of 100 cycles was carried out using the pristine electrolyte and the electrolyte added with 0.002 M Mn^{2+}. As illustrated in Fig. 7a–c, the presence of Mn^{2+} leads to notable enhancements in both CE, with the system demonstrating excellent stability throughout the 100-cycle test. Notably, the pristine electrolyte exhibits a significant capacity fade, retaining only 35% and 39% of its initial charge and discharge capacities, respectively, after 100 cycles. In contrast, the Mn^{2+}-modified electrolyte demonstrates superior capacity retention, maintaining 66% and 73% of its initial charge and discharge capacities under identical cycling conditions. These results indicate that the incorporation of Mn^{2+} effectively mitigates capacity degradation, leading to a substantial improvement in overall battery performance.

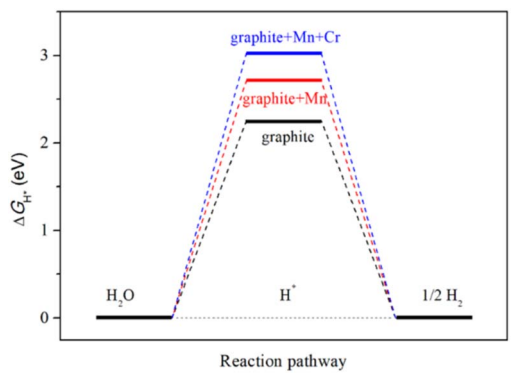

Fig. 8 The calculated HER free-energy diagrams of the bare graphite, Mn absorbed graphite, and Mn–Cr co-adsorbed graphite.

In summary, this study highlights the significant impact of Mn^{2+} concentration on the charge–discharge performance of batteries. By optimizing Mn^{2+} concentration, it is possible to significantly enhance the EE and capacity retention of the battery.

3.2. The mechanism of Mn^{2+} inhibiting hydrogen evolution

To further elucidate the mechanistic role of Mn^{2+} in enhancing the electrochemical performance, we employed DFT calculations to determine the preferential adsorption sites of Mn and their synergistic interactions with Cr species at the negative electrode.

The DFT calculation results show that Mn preferentially adsorbs on graphite hollow site, with the total energy of −668.746 eV/system, which is 0.059 eV/system lower and 0.096 eV/system lower than that on the top site and bridge site, respectively. This adsorption elevates the H adsorption free energy from 2.263 eV (bare graphite) to 2.729 eV, consistent with the experimentally observed shift in HER onset. Furthermore, the Mn–Cr co-adsorbed graphite exhibits the H adsorption free energy of 3.035 eV (Fig. 8). These DFT results provide the information of Mn adsorption sites and its synergistic interaction with Cr species at the negative electrode. DFT calculations reveal that Mn adsorption sites and their incorporation more effectively suppress the HER, in agreement with experimental observations.

4 Conclusions

In this work, Mn^{2+} was introduced as an electrolyte additive to enhance the stability and electrochemical performance of ICRFB. The results demonstrate that Mn^{2+} not only induces a negative shift in HER potential, thereby effectively suppressing parasitic hydrogen evolution, but also I_t also improves the reactivity of Cr^{3+}/Cr^{2+}. This conclusion is further verified in the DFT calculations. These synergistic effects collectively contribute to enhanced charge utilization and cycling stability. The incorporation of 0.002 M Mn^{2+} in the electrolyte led to significant improvements in key battery metrics, increasing the CE from 96.34% to 97.15%, while simultaneously boosting both EE and VE at a current density of 40 mA cm^{-2}. More remarkably, the Mn^{2+}-modified electrolyte exhibits excellent capacity retention, maintaining 73% of its initial discharge capacity after 100

cycles, which is a significant enhancement compared to the observed 39% retention of the unmodified electrolyte. These findings provide valuable insights for the design of high-performance electrolyte additives for ICRFB, highlighting Mn^{2+} as a particularly promising candidate for mitigating capacity fade and improving overall electrochemical efficiency through its dual functionality in both HER suppression and redox reaction enhancement.

Author contributions

Tian-Ying Zhang: investigation, data curation, writing–original draft; Zheng-Rong Niu: conceptualization, formal analysis; Bo Li: writing–review & editing; Yuan-Yuan Cui: software, validation; Nai-Cai Xu: supervision, writing–review & editing, funding acquisition; Xin-Qian Li: writing–original draft; Shao-Ju Bian: resources; Ya-Ping Dong: methodology; Hai-Tao Feng: writing–review & editing, conceptualization, funding acquisition; Yan-Feng Gao: software, validation.

Conflicts of interest

All the authors declare that they have no known competing financial interests or personal relationships that could have appeared to influence the work reported in this paper.

Data availability

All data generated or analysed during this study are included in this published article [and its supplementary information (SI) files]. Supplementary information: the amount of hydrogen produced by the manganese-containing system and the blank control group was measured at 40 mA cm^{-2}, SEM and EDS of graphite felt before charge, XPS spectra of electrode after cycling in electrolyte containing Mn^{2+}. See DOI: https://doi.org/10.1039/d5ra09027j.

Acknowledgements

We are grateful to the 'Kunlun Talents-Science and Technology Leadership Talent' and 'Kunlun Talents High-end Innovation and Entrepreneurship Talents' project (QHKLYC-GDCXCY-2022-027), the research and development of flexible photovoltaic devices and flow battery integration technology, independent deployment project of Qinghai Salt Lake Institute (E260GC0401), and the Science and Technology Plan Projects of Gansu Province (22YF7GG190) supported the work.

References

1 D. G. Nocera, *Acc. Chem. Res.*, 2017, **50**(3), 616–619.
2 N. Mans, H. M. Krieg and D. J. van der Westhuizen, *Adv. Energy Sustainability Res.*, 2024, **5**(3), 2300238.
3 W. Qiu, T. Zhou, R. Zhou, *et al.*, *Chem. Eng. J.*, 2025, 164295.
4 Y. P. Liu, Y. C. Niu, X. C. Ouyang, *et al.*, *Nano Res. Energy*, 2023, **2**, e9120081.
5 M. A. Hannan, S. B. Wali, P. J. Ker, *et al.*, *J. Energy Storage*, 2021, **42**, 103023.
6 E. Ashton, M. Brenton, J. G. Wilson, *et al.*, *ACS Appl. Energy Mater.*, 2025, **8**(2), 1112–1125.
7 S. Park, M. Shin, U. Kunz, *et al.*, *J. Chem. Eng.*, 2024, **41**(8), 2441–2448.
8 C. Y. Sun and H. Zhang, *ChemSusChem*, 2022, **15**(1), e202101798.
9 R. V. Adith, R. p. Naresh, K. Mariyappan, *et al.*, *Electrochim. Acta*, 2021, **388**, 138451.
10 M. L. Fang, Y. Zhang, L. Qiao, *et al.*, *Energy Storage Science and Technology*, 2022, **11**(5), 1358.
11 Z. X. Li, Y. Zhang, S. L. Zheng, *et al.*, *ACS Appl. Energy Mater.*, 2024, **7**(22), 10386–10396.
12 H. Zhang, Y. Tan, J. Y. Li, *et al.*, *Electrochim. Acta*, 2017, **248**, 603–613.
13 Y. C. Niu, S. W. Zeng, G. F. Wu, *et al.*, *Green Energy and Intelligent Transportation*, 2024, **3**(3), 100158.
14 H. X. Che, Y. F. Gao, J. H. Yang, *et al.*, *New Res. Carbon Mater.*, 2024, **39**(1), 131–141.
15 Y. C. Niu, C. Guo, Y. P. Liu, *et al.*, *Nano Res.*, 2024, **17**(5), 3988–3996.
16 C. Y. Sun, H. Zhang, X. D. Luo, *et al.*, *Ionics*, 2019, **25**, 4219–4229.
17 Y. X. Wang, K. Geng, Q. Tan, *et al.*, *ACS Appl. Energy Mater.*, 2022, **5**(12), 15918–15927.
18 E. R. Bai, C. Y. Sun, H. T. Zhu, *et al.*, *Batteries Supercaps*, 2024, **7**(6), e202400007.
19 Y. Q. Li, Q. Wang, K. X. Zhang, *et al.*, *Membr. Sci. Technol.*, 2025, **45**(02), 1–11.
20 M. Bounbaâ, M. Khuili, I. Allaoui, *et al.*, *J. Energy Storage*, 2025, **132**, 117696.
21 M. Wu, M. J. Nan, Y. J. Ye, *et al.*, *Appl. Energy*, 2024, **358**, 122534.
22 Y. Su, H. L. Ren, S. Zhao, *et al.*, *Ceram. Int.*, 2023, **49**(18), 30443–30451.
23 N. Mans, D. van der Westhuizen and H. M. Krieg, *Electrochim. Acta*, 2025, **526**, 146167.
24 X. J. Zhao, X. W. Niu, X. Y. Liu, *et al.*, *Mater. Rep.: Energy*, 2024, **4**(2), 100271.
25 Y. J. Ye, M. Wu, M. J. Nan, *et al.*, *ACS Appl. Energy Mater.*, 2024, **7**(9), 4200–4206.
26 S. L. Wang, Z. Y. Xu, X. L. Wu, *et al.*, *Electrochim. Acta*, 2021, **368**, 137524.
27 S. Y. Niu, S. B. Sun, F. J. Chu, *et al.*, *J. Energy Storage*, 2024, **100**, 113720.
28 Y. H. Deng, Z. X. Li, H. Y. Tan, *et al.*, *J. Electroanal. Chem.*, 2025, **978**, 118874.
29 M. Sotoudeh, S. Baumgart, M. Dillenz, *et al.*, *Adv. Energy Mater.*, 2024, **14**(4), 2302550.